Dalton Transactions

Accepted Manuscript

ROYAL SOCIETY OF CHEMISTRY

www.rsc.org/dalton

Synthesis of Nanorod-FeP@C Composites with Hysteresis Lithiation in Lithium-ion Battery

Jun Jiang,[a,b,c,d] Chunde Wang,[a,b,c,d] Jianwen Liang,[a,b] Jian Zuo,[a] Qing Yang*,[a,b,c,d]

Abstract: Nanorod-FeP@C composites are synthesized via a one-pot solution reaction of ferrocene ($Fe(C_5H_5)_2$) with excess triphenylphosphine (PPh_3) in the sealed vacuum tubes at 390 °C, in which PPh_3 is used as both phosphorus source and solvent in the reaction. The structure and lithium storage performance of the as-prepared nanorod-FeP@C composites is intensively characterized, and it is interesting that the composites exhibit an increased capacity during cycling as serving anode materials for lithium-ion batteries (LIBs). Meanwhile, mechanism investigations reveal that the capacity increase of the composites is resulted from a hysteresis lithiation of the nanostructured FeP phase due to the coating of carbon shell in the composites. Meanwhile, cyclic stability investigation shows that the composites have a very good cyclic stability that shows potential for the composites with long lifespan as a promising kind of anode materials.

Keywords: iron phosphide; transition metal phosphide; carbon coating; hysteresis lithiation; lithium ion battery

Introduction

Transition metal phosphides (TMPs, M = Fe, Co, Ni, etc.), as a new kind of anode materials, have attracted much attention up to date due to their relative higher theoretical capacity as compared to commercial graphite. However, the practical utilization of these materials in the lithium ion batteries (LIBs) system is severely handicapped by their poor capacity retention and unsatisfactory cyclic stability. Recently, detailed investigations have indicated that the drawbacks of most anodes including TMPs compounds are resulted from the poor electrical conductivity and the large volume changes of these phases during conversion reactions in eventual electrochemical lithiation/delithiation processes.[1-4] Hence, it is highly urgent to design effective strategies to buffer

the volume change and improve the conductivity for TMPs. Fortunately, many studies show that assembling with optimal nanostructures[5,6] or hybridizing with carbonaceous materials[7] are effective ways to solve these drawbacks and improve their lithium storage performance. In detail, anode materials in nanostructured forms can improve lithiation kinetics by shortening diffusion lengths and buffer volume expansion of these active materials in both lithiation and delithiation processes. Assume that when carbon is coated on active materials of TMPs as anode, it can serve as a barrier to restrain the aggregation and pulverization of these active materials. And also, the carbon coating can maintain efficient electrical contact with the current collector, and thus increase their structure stability and enhance the kinetics of charge transfer during the charge/discharge processes. Especially, through combining with nanostructure and carbon coating simultaneously, many carbon coated TMP nanostructures exhibit enhanced electrochemical performance as compared to their bulk counterparts. For example, the CoP hollow nanoparticles with carbon coating layer depict good capacity retention and high rate capability (e.g., specific capacity of 630 mAh g^{-1} at 0.2 C after 100 cycles, and a reversible capacity of 256 mAh g^{-1} achieved at a high current rate of 5 C).[8] The cyclic stability and rate capability of Ni_2P are significantly improved after the incorporation of graphene sheets (e.g., after 50 cycles, the Ni_2P/graphene sheet hybrid delivers a capacity of 450 mAh g^{-1} and 360 mAh g^{-1} at a current density of 54.2 and 542 mA g^{-1}, respectively),[9] and so on.[10,11]

Up to now, many methods have been developed to coat carbon on nanomatereials, and it is noted that most routes contain multiple synthetic steps. For instances, a two-step process has been reported for the fabrication of carbon-containing composites, in which early gained carbon nanotubes[12] and graphite oxide[13] are served as a support for active materials via a post deposition/growth process, or a post-annealing treatment has been applied for the preparation of composites with carbon-coating via carbonization of absorbed ligands including alkyl chains from the surfactant onto the targeting active materials under inert atmosphere.[14] It is no doubt that these strategies do work feasibly but it may be inconvenient in most cases. To simply the coating process, we report here a one-pot in situ strategy for the synthesis of iron phosphide nanostructures coated with carbon via a new Ullmann-type reaction, adopted from our early work,[15] with somewhat variations. In detail, the iron transition metal phosphide nanostructures can

be obtained through the reactions of organometallic precursor and triphenylphosphine (PPh_3) in the sealed vacuum tubes, and the coated carbon shells are formed via carbonization of organic by-products in addition to the organometallic precursors themselves. Based on this route, different uniform carbon coated TMPs nanostructures have been achieved.[16]

In the present work, the composites with pure phase FeP nanorods in-situ coated with carbon shells (simplified as nanorod-FeP@C composites) are obtained at 390 °C for 10 h via adjusting molecule ratio of precursors of $Fe(C_5H_5)_2$) and PPh_3 in sealed quartz tube, on the basis of comprehensive characterizations and determination. Interestingly, when they used as the anodes for LIBs, these nanorod-FeP@C composites show a high capacity increase during the cycling. Specifically, the composites deliver a lithium-storage capacity of 330 mA h g^{-1} (based on the total mass of the composites) during the initiative cycles, and then increase to 480 mA h g^{-1} after numbers of cycles with a current density of 30 mA g^{-1}. And detailed investigation reveals that this capacity increasing is caused by a hysteresis lithiation of FeP phase due to the carbon coating in the composites. In addition, these nanorod-FeP@C composites show good cyclic stability and rate capabilities in the cell.

Experimental Section

Materials. Ferrocene ($Fe(C_5H_5)_2 \geq 95\%$) and triphenylphosphine ($PPh_3 \geq 90\%$) are purchased from Alfa Aesar. Solvents of ethanol and toluene are obtained from Shanghai Chemical Reagents Company, China. All reagents are used as received without further purification.

Synthesis of nanorod-FeP@C composites. The synthetic procedures to the nanorod-FeP@C composites are adopted from our previous work[16] with some variations and the details are described as below. In a typical synthesis, a mixture of $Fe(C_5H_5)_2$ (0.093 g, 0.5 mmol) and PPh_3 (0.393 g, 1.5 mmol) are tableted and put into a quartz tube (φ8mm × 150 mm). Then the tube is evacuated and sealed, and loaded into a resistance furnace by a tilt angle of 5°, heated from room temperature to 390 °C at a rate of 2 °C min^{-1}, and kept at this reaction temperature for 10 h. After the tube is naturally cooled to room temperature, the black products are collected, washed with toluene and absolute alcohol several times, and finally dried in a vacuum furnace at 60 °C for further investigation.

Structural Characterization. The purity and phases of the products are identified by X-ray diffraction (XRD) patterns on a Philips X'Pert Pro Super diffractometer with graphite-monochromatized Cu-Ka radiation (λ = 1.54178 Å). The morphologies of the product are examined by field emission scanning electron microscopy (SEM, JEOL JSM-6700F). The transmission electron microscopy (TEM) images, high-resolution TEM (HRTEM) images, and selected area electron diffraction (SAED) patterns are taken on a JEOL-2010 with an accelerating voltage of 200 kV. Raman spectroscopy is carried out on a JY LABRAM-HR confocal laser micro-Raman spectrometer using Ar^+ laser excitation with a wavelength of 514.5 nm. TGA measurements are tested in N_2 and air environment from room temperature to 800 °C at a heating rate of 10 °C min^{-1}. The weight percentage of carbon and hydrogen are characterized by elemental analysis (EA, Elemental vario EL cube, Thermal Conductivity Detector) at pure oxygen atmosphere. The surface structures of the samples are determined by attenuated total reflection Fourier transformed infrared (ATR-FTIR) spectroscopy (Prestige-21, SHIMADZU).

Electrochemical Characterization. Coin-type 2016 cells are assembled in an argon-filled glove box with lithium foil as the counter electrode, celgard 2400 as the separator, and a solution of 1.0 M $LiPF_6$ in ethylene carbonate (EC) /diethyl carbonate (DEC) (1:1 by volume) as the electrolyte. The weight ratio of active materials, acetylene black and poly (vinylidene difluoride) (PVDF) is 8:1:1. After mixed homogeneously with N-methyl-2-pyrrolidone (NMP), the obtained slurry is coated on a copper foil and dried at 100 °C for 12 h in vacuum. The loading of the active materials is in the range of 1.5-2.0 mg. Galvanostatic measurements are tested using a LAND-CT2001A instrument in the potential range of 0.01-3.00 V (vs Li^+/Li) at a designated current density at room temperature. The specific capacities reported in this paper are calculated on the basis of the total weight of composites (iron phosphide + carbon). Cyclic voltammetry is performed at a scan rate of 0.1 mV s^{-1} with an electrochemical workstation (CHI660E).

Results and Discussion

The nanorod-FeP@C composites studied in this work were synthesized by a procedure adopted from our previous work[16] with some variations. Specifically, considering the high boiling point of PPh_3 (~380 °C, 91 kPa), which can serves as phosphorus precursor as well as solvent in the

system, we increased the precursor ratio between PPh_3 and $Fe(C_5H_5)_2$ in the reaction, and the nanorod-FeP@C composites are obtained with high yield. The formation of the highly crystalline FeP phase is identified by XRD pattern, as shown in Figure 1. These diffraction peaks from the products can be indexed to orthorhombic FeP (JCPDF card no. 89-2746) with no indication of other crystal phases. Meanwhile, a broadened scattered peak located near 26° (2θ) suggests the co-existence of carbon in the products.

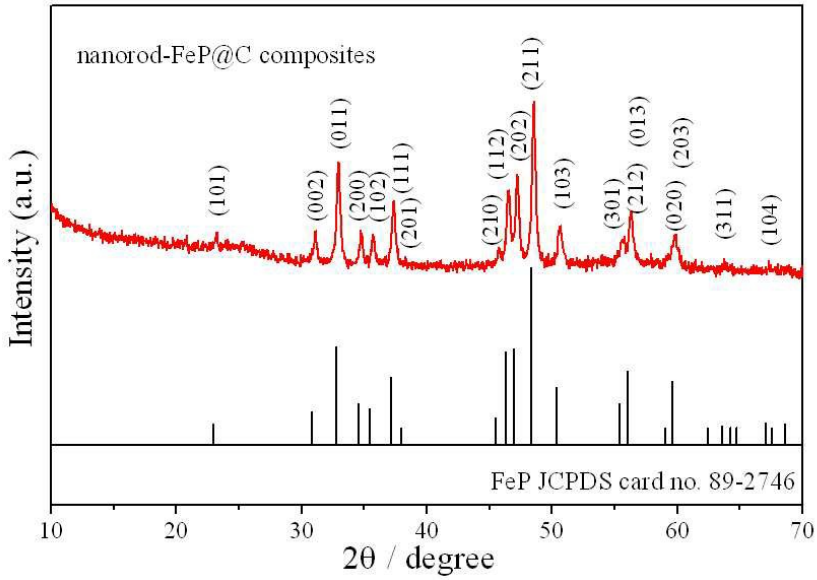

Figure 1. Powder XRD pattern for the nanorod-FeP@C composites (red, top) along with the standard JCPDS card (no. 89-2746) for FeP (black, bottom).

Figure 2a shows a representative SEM image of the as-prepared products, the morphology of the products are spherical with the diameter ranged from several hundred nanometers to few micrometers, and some more SEM images for the products are shown in Figure S1. TEM image (Figure 2b) reveals that these spherical particles are core-shell types, which consist of FeP nanorods clusters and carbon shell. Further structural characterization is implemented to the embedded FeP nanorod. Figure 2c shows the HRTEM image of the nanorod, the lattice fringes are 0.257 nm and 0.302 nm, which corresponds to the planes of (102) and (010), respectively. Meanwhile, besides the FeP lattice, amorphous carbon shells around the nanorod are also detected. The corresponding SAED pattern for the nanorod is shown in Figure 2d, which further confirms the formation of crystalline FeP phase in the composites.

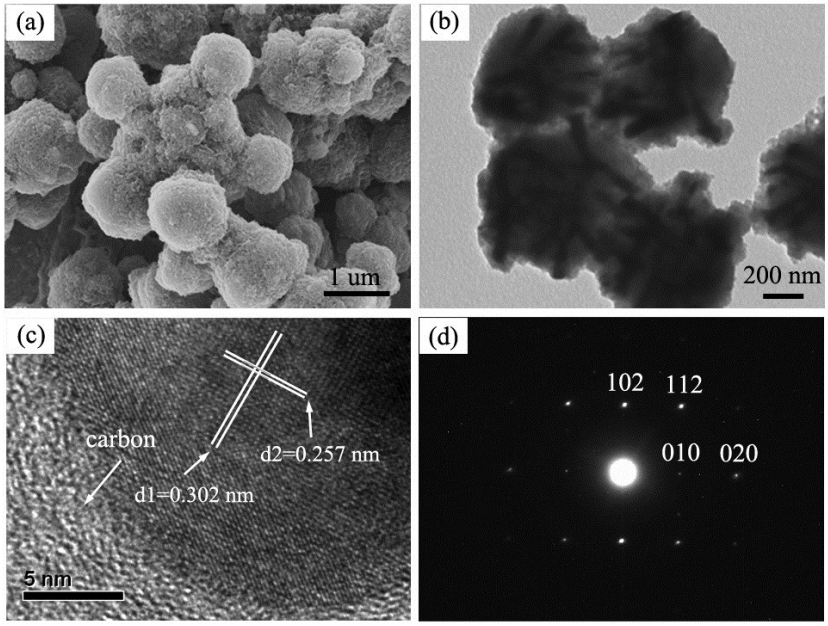

Figure 2. (a) Representative SEM, and (b) TEM images for the as-prepared nanorod-FeP@C composites, (c) HRTEM image of a typical FeP nanorod embedded in the carbon shell, and (d) the corresponding SAED pattern for the nanorod.

The carbon component in the composites is further studied through Raman and ATR-FTIR spectrum. Figure 3a shows a typical Raman spectrum of the composites. Two characteristic peaks located at 1592 and 1352 cm^{-1} are detected, which can be attributed to the G- and D-bands of graphite, respectively.[17] In detail, the G mode of graphite (~1580 cm^{-1}) involves an E_{2g} symmetrical bond stretching motion of pairs of C sp^2 atoms, while the D band (~1350 cm^{-1}) is attributed to the breathing mode of six-membered rings,[18] and the ratio of I (D)/I (G) can be used as an indicator of extent of disordered and ordered graphitic carbon.[19] Figure 3b shows the ATR-FTIR spectra for the composites, it is found that the major bands are located in the region 3000−2850 cm^{-1} , which can be assigned to the C−H stretching modes.[20] So, there are some hydrogen contents in the composite. Another peak located at 1055 cm^{-1} is indexed to P–O stretching mode,[21] which may be caused by surface oxidation.

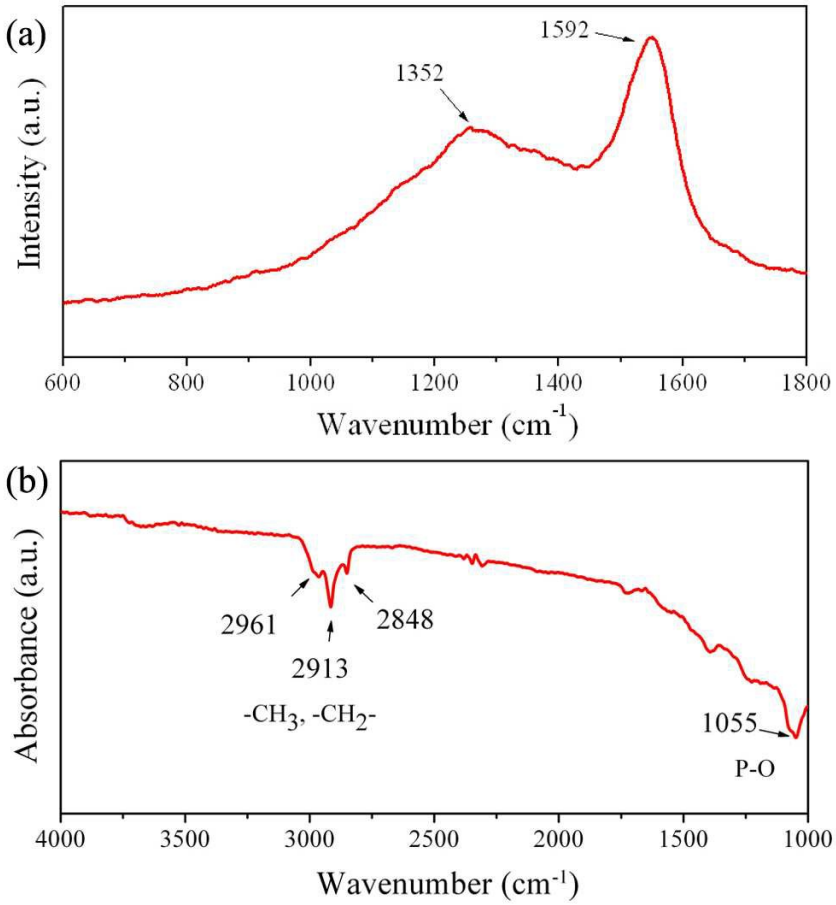

Figure 3. (a) Raman spectrum of the nanorod-FeP@C composites, and (b) ATR-FTIR spectrum of the nanorod-FeP@C composites.

The carbon content in the composites is evaluated by TGA. As seen in Figure 4, under an N_2 atmosphere, the nanorod-FeP@C composites show little weight loss during the whole temperature range, while under an air atmosphere, the thermogravimetric curve of the composites firstly shows a slight weight loss at ~150 °C, probably loss of adsorbates, and then is followed by a slight weight gain from ~200 °C to ~400 °C, which may be resulted from the oxidation of FeP. When the temperature is over 400 °C, the products show a sharp loss, which can be ascribe to the oxidation of carbon content in the composite until the temperature reached ~550 °C, in this process, almost 50 wt.% of the products is lost. Considering the coexistence of carbon and hydrogen elements in the composites, the accurate carbon and hydrogen content in the composites are detected by elemental analysis, and the values are 50.70 wt.% and 2.59 wt.%, respectively.

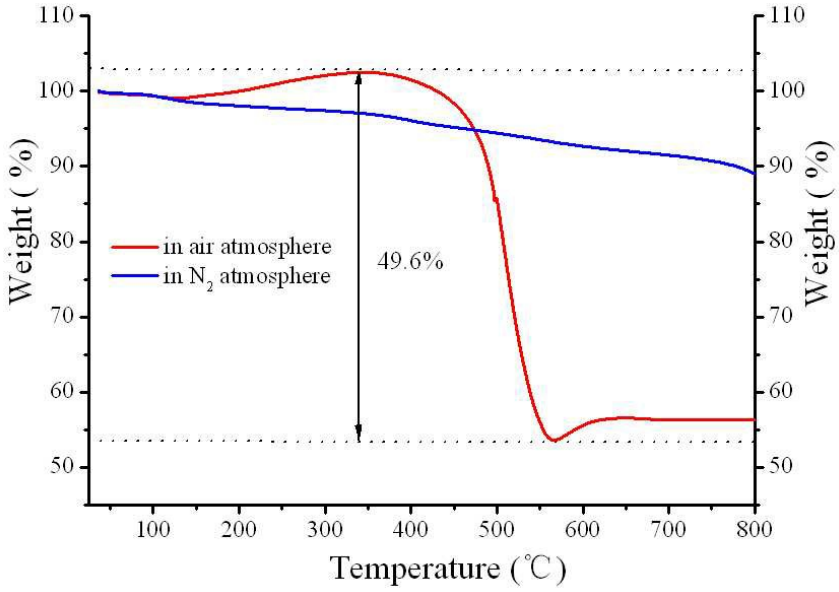

Figure 4. TGA curves of the nanorod-FeP@C composites under the N_2 and air atmosphere from room temperature to 800 °C at a heating rate of 10 °C min^{-1}.

The electrochemical performances of the nanorod-FeP@C composites are performed with Li metal as the counter electrode and 1.0 M $LiPF_6$ in ethylene carbonate (EC)/diethyl carbonate (DEC) (1:1 by volume) as electrolyte in the coin-type cells. Figure 5a shows the cycle performance of the nanorod-FeP@C composites between 0.01 and 3.0 V at a current density of 30 mA g^{-1}, and the capacity is calculated based on the total mass of the composites (iron phosphide with carbon). In the first cycle, the discharge and charge capacities of the composites are 986 and 277 mA h g^{-1}, respectively, which leads to a low initial coulombic efficiency (CE) of 28.1%. Subsequently, the capacity of the composites keeps at around 330 mA h g^{-1} until the 40th cycles. Interestingly, between the 40th and 50th cycles, the capacity of the composites shows an obvious ascending trend. After 50th cycles, the capacity of the composites increases to around 460 mA h g^{-1}. Finally, after 200th cycles, the capacity of the composites maintains at around 480 mA h g^{-1}. The corresponding charge-discharge voltage profiles of the composites at the same test condition are shown in Figure 5b. Upon the initial discharge, a narrow platform appears at approximately 1.0 V, which may be ascribed to the formation of a solid electrolyte interlayer (SEI) film and disappears in the follow cycles, and then a broad platform appears below 0.2 V. While on the charge process, an unconspicuous platform started from 1.5 V can be detected. Except the

platform located at 1.0 V, the platforms during the subsequent charge-discharge voltage profiles are still in the same position. However, as the cycle number increases, a new couple of platforms located at 0.6 and 1.1 V emerge during the discharge-charge process, especially, after 50 cycles, the new emerged platforms are obviously observed. And even after 200 cycles, these new platforms still exist. So, the new emergent platforms probably contribute to the increase of the capacity.

In order to investigate the formation mechanism of the platforms, the cyclic voltammetry (CV) of the composites are performed between the potential ranges of 0.01-3.0 V (vs Li^+/Li) at a scanning rate of 0.1 mV s^{-1}. Figure 5c shows the CV curves of the first, second, and third discharge/charge processes. In the first cycle, a cathodic peak between 0.8 and 0.7 V, which disappearing in the following cycles can be ascribed to the formation of the SEI film.[22] Another cathodic peak located at 0.01~0.5 V with a sharp corner is observed. However, during the charge process, no distinguishable anodic peaks except a long bump from 0.8 V to 3 V can be observed. Besides the cathodic peak located between 0.8 and 0.7 V, the CV curves keep the same in the second and third cycle process. Referring to previous reports,[23-25] the lithiation mechanism of iron phosphide in the first discharge process can be depicted as follows: FeP is directly conversing to Li_3P and Fe metal ($FeP + 3Li \rightarrow Li_3P + Fe^0$) with the potential platform at 0.1 V. Considering that the lithiation of both FeP phase and carbon take place under 0.2 V, a galvanostatic intermittent titration technique (GITT) test in the first lithiation is conducted, and then the active materials is characterized by XRD to deduce the potential Li-FeP reaction in the cell. As seen in Figure S2a, the GITT curves of the composites show a platform between 1.0 V and 0.8 V, and a long platform below 0.2 V. Meanwhile, except two peaks for Cu foil, there are no other distinguishable peaks in the XRD pattern (Figure S2b). So, the long lithiation platform below 0.2 V should contain the lithiation of both FeP phase and carbon in the composites. However, in the following charge process, the CV curve in Figure 5b shows unconspicuous peaks, which is also observed in the subsequent cycles. As note, the CV curves in Figure 5b are very similar to the CV curves of the electrochemical reaction between lithium and disordered carbon, of which lithium uptake occurs close to 0 V (vs Li^+/Li) whereas lithium desertion occurs at much more positive potentials, and the extent of this charge and discharge potential hysteresis is proportional to the hydrogen content in

the carbon.[26,27] Considering the high carbon and hydrogen content in the composites, the CV curves in Figure 5c can be attributed to the electrochemical reaction between lithium and the carbon shell in the composites. Meanwhile, the intercalation and deintercalation process of disordered carbon material is different from the traditional carbon in the cell,[28,29] which can be expressed as $6C + xLi + xe^- \rightarrow Li_xC_6$, and the x in Li_xC_6 can reach 1.2~3.0. So a high specific capacity of the carbon in our composites is also presented. After 100 cycles in the current density of 30 mA g^{-1}, another CV test (Figure 5d) at the same scan rate with the former is conducted to verify the emergent platforms. As expected, a new couple of peaks located at 0.6 and 1.2 V are observed as compare to the result in Figure 5c. However, as compared to the reports[23] of the location of peaks for the FeP phase (a conversion reaction of $Li_3P + Fe \rightarrow Li_xFeP$ with the potential platform at 0.92 V/0.21 V and an insertion/desertion reaction $Li_xFeP \rightarrow FeP + xLi$ with the potential platform at 1.05 V/0.55 V), the positions of peaks in our study do not match with them. To further characterize the products during the charge/discharge process, we collect the XRD pattern (Figure S3) and XPS spectra (Figure S4) of the active materials (the emerging platforms are already observed) under a state of fully discharge and charge. However, the signals form XRD pattern are amorphous products and the signals from XPS spectra are too weak. So, it is difficult to detect the signal of the active material from these ex-situ techniques. Herein, we carry another CV with a much slower scan rate as well as GITT test to observe the location of the peaks in the curve. As shown in Figure S5a-5b, the peaks in the CV plot are in good agreement with the platforms in the GITT curves. Meanwhile, it is easy to find that the peaks in the CV curve are good agreement with the results from reaction between Li and phosphorous.[30] Hence, from the above investigations and observed evidences, with the current density of 30 mA g^{-1} the initial electrochemical reaction in the cell is primary involved with the carbon shell and lithium, and the FeP phases are kinetic limitation to lithiation completely in the initial cycles and have to react with lithium gradually along with the cycle numbers. Finally, the electrochemical reaction transforms to lithium with phosphorous and disordered carbon in the cell. So, a hysteresis lithiation of FeP phases is observed in the cell. In addition, the rate capability of the composites is plotted in Figure 5e. The rate capability of the composites is directly conducted after 200 cycles at the current density of 30 mA g^{-1}. Specifically, the composites deliver discharge capacities of around 480, 400,

230, 80, and 50 mA h g^{-1} at current densities of 30 mA g^{-1}, 60 mA g^{-1}, 150 mA g^{-1}, 300 mA g^{-1}, and 600 mA g^{-1}, respectively. And the capacity of the composites can recover when the current density is reduced from 600 mA g^{-1} to 30 mA g^{-1}.

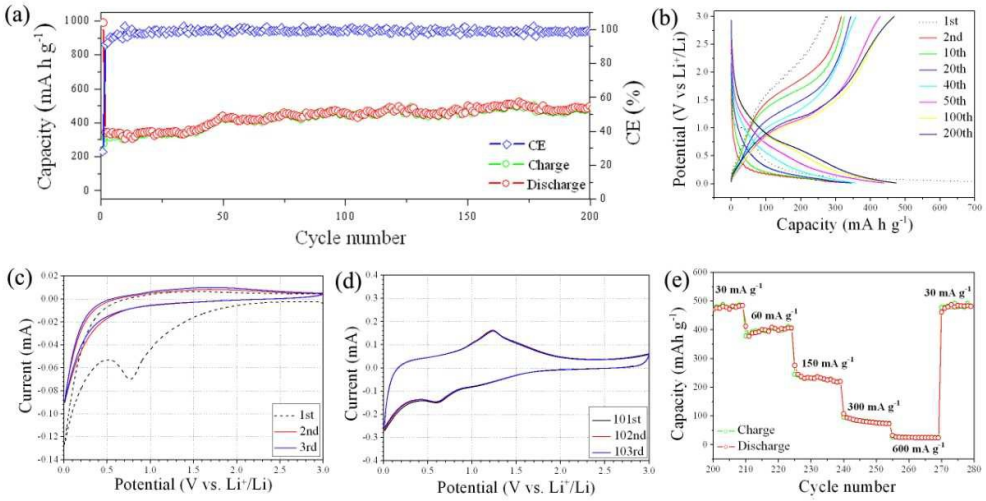

Figure 5. (a) Cycling performances of the nanorod-FeP@C composites at a current density of 30 mA g^{-1}, (b) charge-discharge voltage profiles of the nanorod-FeP@C composites at the current density of 30 mA g^{-1} for the 1st, 2nd, 10th, 20th, 40th, 50th, 100th and 200th cycles, (c) cyclic voltammetries of the nanorod-FeP@C composites between 0.01 and 3 V at a scan rate of 0.1 mV s^{-1} for the 1st, 2nd, and 3rd cycles, (d) cyclic voltammetries of the nanorod-FeP@C composites between 0.01 and 3 V at a scan rate of 0.1 mV s^{-1} after 100 cycles at a current density of 30 mA g^{-1}, and (e) rate capability of the composites after 200 cycles at the current density of 30 mA g^{-1}.

To further confirm the hysteretic lithiation of the FeP phase in the composites, ex situ techniques, including XRD, SEM and TEM are employed to characterize the composites after different cycle numbers in its fully charged state. Figure 6 shows the XRD pattern of the composites after 5 and 100 cycles, respectively. Besides a broad peak near 20° (2θ), which can be indexed to the signal of porous carbon[31] and further identified by XRD as shown in Figure S6, other peaks in the curve match well with the peaks from orthorhombic phase FeP (89-2746). And the signal of porous carbon is also observed in the XRD pattern of the composites after 100 cycles, but, the relative intensity of the peaks indexed to FeP phase are drastically weakened, as compare to the case after 5 cycles. The corresponding SEM and TEM images of the composites after 5 and 100 cycles are showed in Figure 7, respectively. Obviously, after 5 cycles, the morphology of the

composites (Figure 7a) fundamentally maintains the same and many FeP nanorods are still coated with the carbon matrix (Figure 7b). While after 100 cycles, the composites are pulverized (Figure 7c), and the carbon matrix becomes a network structure and the FeP nanorods in the carbon matrix are hardly observed (Figure 7d). To investigate the influence of current density for the hysteresis lithiation of FeP phases in the cell, the composites with a current density of 10 and 60 mA g^{-1} are also tested (Figure S7). With a current density of 10 mA g^{-1}, the composites (Figure S7a) demonstrate a discharge capacity of ~500 mA h g^{-1} in the second cycle and maintain almost the same capacity after 10 cycles. Meanwhile, from the corresponding charge-discharge voltage profiles of the composites (Figure S7b) a platform between 0.7 V and 0.5 V is already observed. While for the electrode with a current density of 60 mA g^{-1}, the composites deliver a discharge capacity of ~280 mA h g^{-1} in the second cycle and the capacity increases to ~400 mA h g^{-1} after 200 cycles in the cell (Figure S7c). Moreover, represented by the corresponding charge-discharge voltage profiles of the composites (Figure S7d), the platform between 0.7 V and 0.5 V can be observed only after 150th discharge and charge processes in the cell. So, the existing FeP phase in Figure 6a can be attributed to the kinetic limitation to lithiation the FeP phase completely during the initiative cycling in the cell. Except the hysteretic lithiation of FeP phase in the cell, which provides increase capacity, capacitance of the double layer also should be taken into consideration. As the cycle number increasing, the carbon matrix in the composites becomes a network structure (as seen in Figure 7d), the surface area of the composites would be enlarged. So, the capacitance of the double layer is also increased along with the cycle number. Herein, according to the previous reports,[32] the peak current obeys a power-law relationship with the sweep rate ($i = av^b$) in the CVs, where a b-value of 0.5 would indicate that the current is controlled by semi-infinite linear diffusion, a value of 1 indicates that the current is surface-controlled. Hence, we measure the CVs with a scan rate from 0.02 to 1 mV s-1 of the composites after 200 cycles (Figure S8a), and a plot of log (i) versus log (v) is shown in Figure S8b. From the as-obtained slope in Figure S8b, the b-value is ~0.6 in the cell. So, there are some capacitances of the double layer for the overall capacities. For comparison, FeP@C nanocables are also synthesized and tested (Figure S9-S11). They also show a hysteresis lithiation of FeP phase in the cell, but, due to the difference of morphology of carbon shell in the products, the capacity of the FeP@C nanocables are inferior to

that of the nanorod-FeP@C composites. Herein, the hysteresis lithiation may be a common phenomenon for the materials synthesized by the same routes.

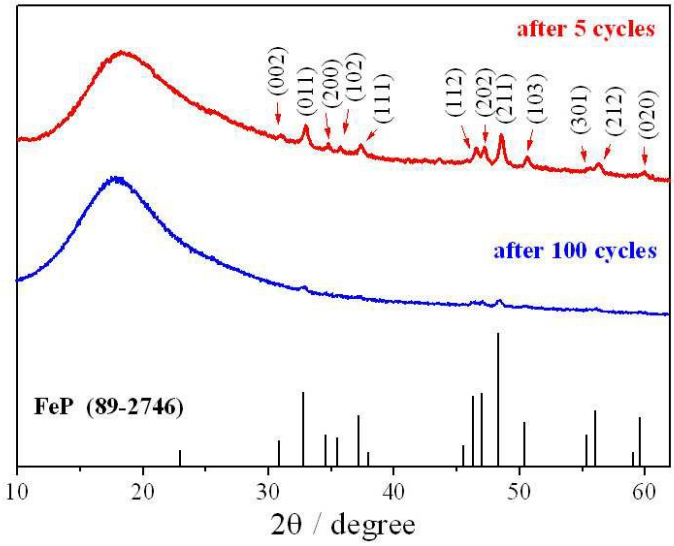

Figure 6. Ex situ XRD patterns of the nanorod-FeP@C composites after 5 and 100 cycles, respectively.

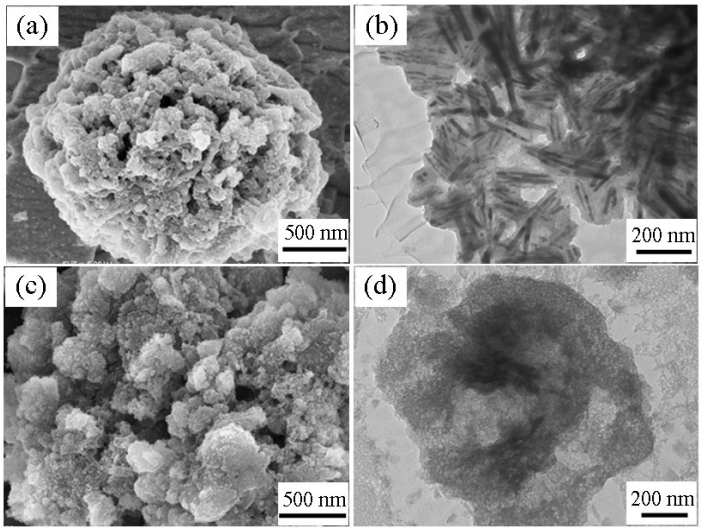

Figure 7. (a), (b) SEM and TEM images of the nanorod-FeP@C composites after 5 cycles, and (c), (d) after 100 cycles.

Conclusion

In summary, the nanorod-FeP@C composites are synthesized with excess PPh_3 in the reaction, which is served as P source and solvent. Comprehensive characterizations show that a high carbon and hydrogen content is observed, which are coating the FeP nanorods in the composites. Due to

the affect of these carbon shells, the electrochemical process of the composites as anode materials in lithium-ion batteries shows a hysteresis lithiation phenomenon that the electrochemical process related to the FeP phase is hysteretic by the coated carbon in the composites. For the electrochemical performance of these composites, they deliver a starting specific capacity of 330 mA h g^{-1}, and then improve to 480 mA h g^{-1} after 200 cycles at a current density of 30 mA g^{-1}. From the electrochemical investigations, the capacity of the FeP phases in the composites is less than their theoretical capacity, but a high capacity of the carbon shell in the composites is observed. Meanwhile, with the auxiliary of carbon shell, these composites exhibit a good cyclic stability. The synthesis route combined with the hysteresis lithiation phenomenon in the present work may provide new insights in the lithium-ion batteries.

Acknowledgments

This work was supported by the National Nature Science Foundation of China (51271173, 21071136), the National Basic Research Program of China (2012CB922001). We thank Prof. Shuji Ye at USTC for his technical assistance on ATR-FTIR measurements.

Notes and references

[a] Hefei National Laboratory of Physical Sciences at the Microscale (HFNL), University of Science and Technology of China (USTC), Hefei 230026, Anhui, P. R. China.

[b] Department of Chemistry, USTC, Hefei 230026, Anhui, P. R. China.

[c] Laboratory of Nanomaterials for Energy Conversion (LNEC), USTC, Hefei 230026, Anhui, P. R. China.

[d] Synergetic Innovation Center of Quantum Information & Quantum Physics, USTC, Hefei 230026, Anhui, P. R. China.

Corresponding author: E-mail: qyoung@ustc.edu.cn; Fax: +86-0551-63606266; Tel: +86-0551-63600243.

Electronic Supplementary Information (ESI) available: Figure. S1-S11. See DOI: 10.1039/b000000x/

1 D. C. S. Souza, V. Pralong, A. Jacobson and L. F. Nazar, *Science*, 2002, **296**, 2012－2015.

2 V. Pralong, D. C. S. Souza, K. T. Leung and L. F. Nazar, *Electrochem. Commun.,* 2002, **4**, 516－520.

3 R. Alcantara, J. L. Tirado, J. C. Jumas, L. Monconduit and J. Olivier-Fourcade, *J. Power Sources*, 2002, **109**, 308－312.

4 J. Cabana, L. Monconduit, D. Larcher and M. R. Palacin, *Adv. Mater.*, 2010, **22**, 170－192.

5 P. G. Bruce, B. Scrosati and J.-M. Tarascon, *Angew. Chem., Int. Ed.,* 2008**, 47**, 2930－2946.

6 S. Boyanov, K. Annou, C. Villevieille, M. Pelosi, D. Zitoun and L. Monconduit, *Ionics,* 2008, **14**, 183－190.

7 X. Ji, K. T. Lee and L. F. Nazar, *Nat. Mater.,* 2009, **8**, 500－506.

8 D. Yang, J. Zhu, X. Rui, H. Tan, R. Cai, H. E. Hoster and Q. Yan, *ACS Appl. Mater. Interfaces,* 2013, **5**, 1093－1099.

9 Y. Lu, X. Wang, Y. Mai, J. Xiang, H. Zhang, L. Li and S. X. Mao, *J. Phys. Chem. C,* 2012, **116**, 22217－22225.

10 Y. Lu, J. P. Tu, J. Y. Xiang, X. L. Wang, J. Zhang, Y. J. Mai and S. X. Mao, *J. Phys. Chem. C,* 2011, **115**, 23760－23767.

11 Z. Liang, R. Huo, S. Yin, F. Zhang and S. Xu, *J. Mater. Chem. A,* 2014, **2**, 921－925.

12 S.-W. Kim, D.-H. Seo, H. Gwon, J. Kim and K. Kang, *Adv. Mater.,* 2010, **22**, 5260－5264.

13 S. Yang, X. Feng, S. Ivanovici and K. Mullen, *Angew. Chem., Int. Ed.,* 2010, **49**, 8408－8411.

14 S. Carenco, C. Surcin, M. Morcrette, D. Larcher, N. Mézailles, C. Boissière and C. Sanchez, *Chem. Mater.,* 2012, **24**, 688－697.

15 J. Wang, Q. Yang, Z. Zhang and S. Sun, *Chem. Eur. J.,* 2010, **16**, 7916－7924.

16 J. Wang, Q. Yang, Z. Zhang, *J. Phys. Chem. Lett.,* 2009, **1**, 102－106.

17 C. Lee, X. Wei, J. W. Kysar and J. Hone, *Science*, 2008, **321**, 385－388.

18 G. M. Fuge, P. W. May, K. N. Rosser, S. R. J. Pearce and M. N. R. Ashfold, *Diamond Relat. Mater.,* 2004, **13**, 1442－1448.

19 S. C. Lyu, B. C. Liu, C. J. Lee, H. K. Kang, C. W. Yang and C. Y. Park, *Chem. Mater.*, 2003,

15, 3951－3954.

20 T. S. Grimes, G. X. Tian, L. F. Rao and K. L. Nash, *Inorg. Chem.,* 2012, **51**, 6299－6307.

21 E. S. Gawalt, G. Lu, S. L. Bernasek and J. Schwartz, *Langmuir*, 1999, **15**, 8929–8933.

22 Y. S. Hu, P. Adelhelm, B. M. Smarsly, S. Hore, M. Antonietti and J. Maier, *Adv. Funct. Mater.,* 2007, **17**, 1873－187.

23 S. Boyanov, J. Bernardi, F. Gillot, L. Dupont, M. Womes, J. M. Tarascon and M. L. Doublet, *Chem. Mater.,* 2006, **18**, 3531－3538.

24 S. Boyanov, M. Womes, L. Monconduit and D. Zitoun, *Chem. Mater*., 2009, **21**, 3684－3692.

25 S. Boyanov, D. Zitoun, M. Ménétrier, J. C. Jumas, M. Womes and L. Monconduit, J. *Phys. Chem. C,* 2009, **113**, 21441－21452.

26 T. Zheng, Y. Liu, E. W. Fuller, S. Tseng, U. Von Sacken and J. R. Dahn, *J. Electrochem. Soc.* 1995, **142**, 2581－2590.

27 M. Winter, J. O. Besenhard, M. E. Spahr and P. Novak, *Adv. Mater.,* 1998, **10**, 725－763.

28 F. Bonino, S. Brutti, P. Reale, B. Scrosati, L. Gherghel, J. Wu and K. MüLLEN, *Adv. Mater.,* 2005, **17**, 743－746.

29 H. Zhou, S. Zhu, M. Hibino, I. Honma and M. Ichihara, *Adv. Mater.,* 2003, **15**, 2107－2111.

30 J. Qian, D. Qiao, X. Ai, Y. Cao and H. Yang, *Chem. Commun.,* 2012, **48**, 8931－8933.

31 L. Wang, X. He, J. Li, W. Sun, J. Gao, J. Guo and C. Jiang, *Angew. Chem., Int. Ed.,* 2012, **51**, 9034－9037.

32 V. Augustyn, J. Come, M. A. Lowe, J. W. Kim, P. L. Taberna, S. H. Tolbert and B. Dunn, *Nat. Mater.*, 2013, **12**, 518－522.

Graphical Abstract

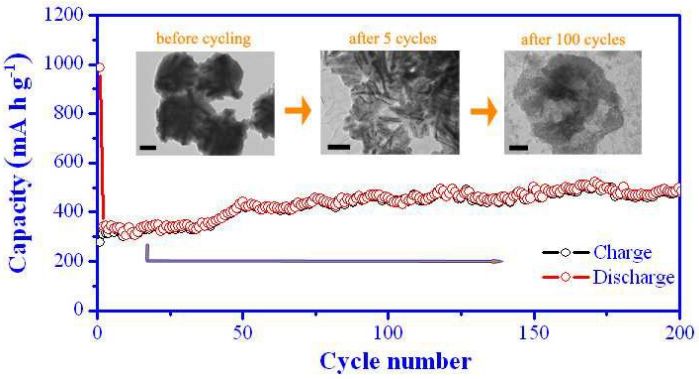

We report a facile one-pot synthetic route to nanorod-FeP@C composites, and their performances as anode for lithium ion battery have been investigated.